HIGH-SPEED COMPOUND ROTORCRAFT FLIGHT CONTROL DESIGN AND ASSESSMENT

Johannes Wartmann, Peter Weiand, Kagan Atci
German Aerospace Center (DLR), Institute of Flight Systems, Braunschweig, Germany

Abstract

To support current defense initiatives such as NATO's Next Generation Rotorcraft Capability, which aims for the development and fielding of rotorcraft with higher maximum airspeed, the German Aerospace Center (DLR) has been conducting various studies regarding high-speed-capable rotorcraft configurations. Using DLR's Integrated Rotorcraft Initial Sizing environment, a high-speed compound rotorcraft was sized and designed to achieve airspeeds above 240 knots. The configuration features a main rotor, a tail rotor, a pusher propeller, a wing, and an empennage. The wings and empennage are equipped with additional aerodynamic control surfaces. This paper briefly presents the designed high-speed rotorcraft and its linear model properties. The focus of the paper is the development of an explicit model-following flight control system for the compound rotorcraft across the entire flight envelope. The corresponding feedback gains are optimized with MATLAB *systune*. The utilized optimization goals and their relation to ADS-33E criteria are examined. The designed flight control system is mostly predicted to achieve a Level 1 ratings.

NOTATION

K	system gain
M_q	example of stability derivative
M_{δ_x}	example of control derivative
I	mass moment of inertia tensor
R	main rotor radius
s	Laplace variable
$\boldsymbol{u}$	control allocation input
u, y	system input and output
x, y, z	Cartesian coordinates
V_{tas}	true airspeed
v_z	vertical velocity
$\boldsymbol{\delta}$	actuator control inputs
$\boldsymbol{\delta}_{\text{s}}$	pilot stick inputs
δ_x, δ_y	longitudinal, lateral cyclic deflection
δ_0	(main rotor) collective deflection
δ_p	tail rotor collective deflection
δ_{thr}	pusher propeller collective deflection
δ_{ele}, δ_{rud}	elevator, rudder deflection
δ_{ail}, δ_{flp}	aileron, flap deflection
$\delta_{\omega_{\text{MR}}}$	main rotor speed
$\delta_{x_{\text{s}}}$	longitudinal cyclic stick input
ζ	damping ratio
τ	time delay
ϕ, θ	roll and pitch attitudes
ω_x	natural frequency x (with index)
ACAH	Attitude Command / Attitude Hold
CA	control allocation
CM	command model
DLR	Deutsches Zentrum für Luft- und Raumfahrt (German Aerospace Center)
DRB, DRP	disturbance rejection bandwidth, peak
EMF	explicit model-following
FF	feedforward
FLRAA	Future Long-Range Assault Aircraft
FVL	Future Vertical Lift
HOST	Helicopter Overall Simulation Tool
HQ	handling qualities
HSR	high-speed rotorcraft
IRIS	Integrated Rotorcraft Initial Sizing
MOI	moments of inertia
MR, TR	main rotor, tail rotor
MTE	Mission Task Element
NATO-GR	NATO Generic Rotorcraft
NGRC	Next Generation Rotorcraft Capability
RCAH	Rate Command / Attitude Hold

Presented at the 51st European Rotorcraft Forum, Venice, Italy, 9-12 September, 2025.

1. INTRODUCTION

High-speed configurations represent a significant advancement in rotorcraft design, particularly relevant within the defense context. Achieving higher maximum airspeeds is increasingly crucial for rapid area coverage and for evading radar detection, especially at low altitudes. Notable examples of such high-speed rotorcraft (HSR) research include NATO's Next Generation Rotorcraft Capability (NGRC) project and the U.S. Future Vertical Lift (FVL) initiative. NATO's NGRC is exploring the potential for higher speeds in the development of a new medium-weight rotorcraft, with projected flight speeds between 180 and 220 knots. Similarly, the Future Long-Range Assault Aircraft (FLRAA) program within FVL targets this weight class, aiming for speeds between 250 and 280 knots.

The German Aerospace Center (DLR) supports NGRC activities through dedicated, ongoing research in defense technology. A conception study to assess the advantages and disadvantages of a high-speed-capable rotorcraft configuration for a specific mission scenario was conducted [1]. DLR's rotorcraft design environment, Integrated Rotorcraft Initial Sizing (IRIS), serves as the main framework for model initialization, sizing, and analysis within the recent studies. Further studies are also focused on the conceptual design of new Helicopter Emergency Medical Services (HEMS) configurations [2].

To cover FLRAA applicants design concepts, the U.S. Army Aviation Development Directorate developed two generic configurations: a coaxial rotorcraft with a pusher propeller, and a tiltrotor [3]. Flight control systems were developed for both models to investigate the resulting handling qualities (HQ) of the models and generally to accelerate the development of HQ for high-speed configurations [4, 5]. Furthermore, a winged single main rotor / tail rotor helicopter with lower design speed and take-off mass was also discussed [6].

For DLR's conceptual HSR study, a new compound rotorcraft configuration was compared with a reference conventional helicopter. The comprehensive code Helicopter Overall Simulation Tool (HOST), developed by Airbus Helicopters [7], is used internally within IRIS for the computation of the flight mechanics model. Furthermore, the resulting helicopter models were gradually revised and extended for non-linear time-domain simulation. The studied HSR configuration currently features an off-loaded main rotor, wings, a tail rotor, and a pusher propeller to achieve flight speeds of over 240 knots. Aerodynamic control surfaces are incorporated for the wings, as well as the vertical and horizontal stabilizers, and rudder to minimize the necessary control inputs on the main rotor during high-speed flight.

This paper provides an overview of the development of the flight controls of the HSR, beginning with the conceptual design and modeling of its flight mechanics in Section 2. The design approach, including the reference configuration and requirements, is described and the resulting flight mechanics model is detailed and examined concerning important derivatives and eigenvalues. The main focus of the paper is the design of an explicit model-following (EMF) flight control system for the HSR across the entire speed range. The architecture of the flight control system is described in detail in Section 3. The optimization process of the flight control parameters, the corresponding goals, and the assessment of the designed flight control system using quantitative handling qualities and robustness criteria are presented in Section 4.

2. HIGH-SPEED ROTORCRAFT MODEL

2.1. Conceptual Design

The extension of the flight envelope for a rotary wing aircraft is critically dependent on the choice of configuration. Going beyond the speed limits of conventional helicopters, three reliable configuration types can be considered: a convertible or tilt rotor configuration, a coaxial lift-offset configuration, and a conventional single main rotor compounded with a wing. The latter two are extended by additional propulsive components, e.g. pusher propellers.

In the previous study [1], a conventional medium-weight reference helicopter configuration, called NATO Generic Rotorcraft (NATO-GR), was modified into a compound rotorcraft with the intention of increasing the flight speed by approximately 50% in comparison to NATO-GR. The NATO-GR was modeled on the basis of an UH-60, based on public available data [8] reaching up to 160 knots.

The maximum flight speed of a conventional helicopter is limited by two events occurring in the main rotor: rising transonic drag on the advancing blade side and stall due to high angles of attack on the retreating blade side, as analyzed in [1] for the NATO-GR. To increase the maximum flight speed and counter the increasing drag, the propulsive force must be decoupled from the main rotor through a propeller or similar. The second measure comes into play when a critical Mach number is reached on the advancing blade side: the rotational speed of the main rotor is reduced to keep the Mach number below a critical value. Hence, an area with high dynamic pressure on the advancing blade side generates at the cost of a larger area with reversal flow on the retreating blade side. A reduced blade loading is an approach that helps balancing the two rotor sides. As a result of the reduction of rotational speed and blade loading, the main rotor shows a substantial reduction in thrust and can no longer carry the weight of the vehicle. In this case, the required lift is complemented with wings, when the rotor thrust is limited at higher speeds. To improve vehicle maneuverability without increasing the load on the main rotor at fast forward flight, control surfaces on the wings and stabilizers are applied.

The high-speed configuration being designed aims to fulfill similar mission requirements at higher airspeeds as those of the NATO-GR. Given the military context, a pusher propeller at the tail generates propulsion, ensuring that the side doors remain unobstructed by rotating elements and improving ground handling. This configuration resulted in a compound rotorcraft referred to as the high-speed rotorcraft. It features a main rotor, a tail rotor, a pusher propeller at the vehicle's tail, wings, and an empennage. The HSR configuration is depicted in Figure 3.

The chosen HSR configuration poses a number of challenges: Firstly, heavy components are located far behind the conventional helicopter's center of gravity, and secondly, a single propeller generates strong additional roll moments. In addition, the position of the tail rotor must be located further out from the rotorcraft symmetry plane due to the propeller at the tail. From a scientific point of view, such a configuration is challenging, and has not yet been comprehensively analyzed. Nonetheless, other configurations with two lateral thrust generators, such as the Airbus Helicopters RACER [9], can dispense with the need of a tail rotor and may be advantageous from an engineering point of view.

An air assault profile was chosen as a representative design mission to analyze the flight performance of the NATO-GR and the HSR. The air assault mission, as shown in Figure 1, was computed with a mission radius of 201 km and applied the maximum speed of 160 knots for NATO-GR and 240 knots for the HSR. Modeling and analysis of the NATO-GR, as well as initialization, sizing, and analysis of the HSR, was conducted with IRIS.

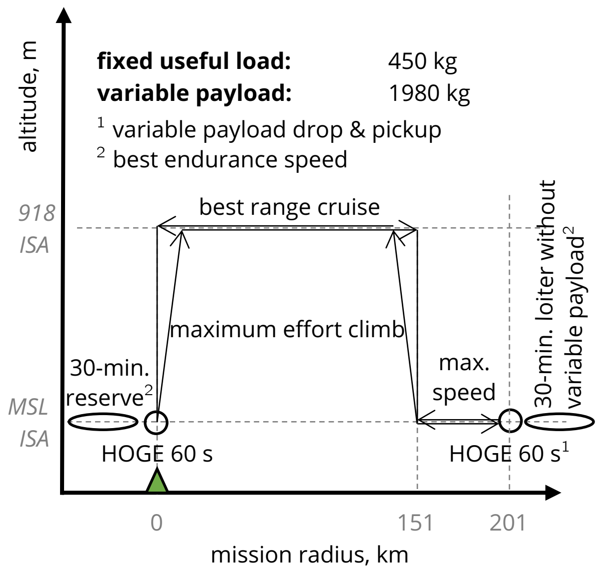

Figure 1: Design mission profile "Air Assault", see [1].

The results show a strong increase in the rotorcraft dimensions, with a rise in the maximum take-off mass by +76.4%. The specifications of the NATO-GR and the sized HSR configuration are compared in Table 1.

Table 1: Main specifications of NATO-GR and the HSR.

Specification	NATO-GR	HSR
Maximum take-off mass	9926 kg	17 507 kg
Basic empty mass	6191 kg	12 348 kg
Fuel mass	1305 kg	2729 kg
Payload mass	2430 kg	
Main rotor radius	8.18 m	10.86 m
Tail rotor radius	1.68 m	2.18 m
Propeller radius	-	2.13 m
Wing area	-	19.89 m^2
Maximum range	619 km	704 km
Maximum airspeed	160 knots	>240 knots

A comparison of the required power in level flight can be found in Figure 2 for the NATO-GR and the HSR including the required speed interval defined by NGRC. The extension of the flight envelope from 160 knots to 240 knots exceeds the NGRC requirements by 20 knots. Here, the curve of the HSR configuration shows an increase of flight speed by 50% compared to the NATO-GR reference along with a threefold increase in power requirement at 240 knots.

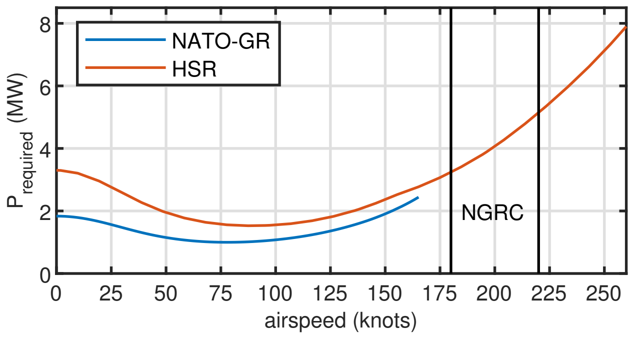

Figure 2: Power required of NATO-GR and the HSR in level flight.

This tremendous increase in required power for the installed engines shifts the efficiency of the vehicle to higher flight speeds, making the HSR inefficient within the envelope of the reference configuration. These findings were incorporated in a revised HSR model generation, where a new rotor design was conducted. Further investigations focused on the influence of different maximum flight speeds and mission radii [10]. For the purpose of this paper, the first design of the HSR configuration, as presented in [1], set the baseline for the development of the flight control system. The specifications of the used HSR iteration, as shown in Table 1, are representative for the studies in this paper. Figure 3 shows the sized HSR configuration including length dimensions and the center of gravity.

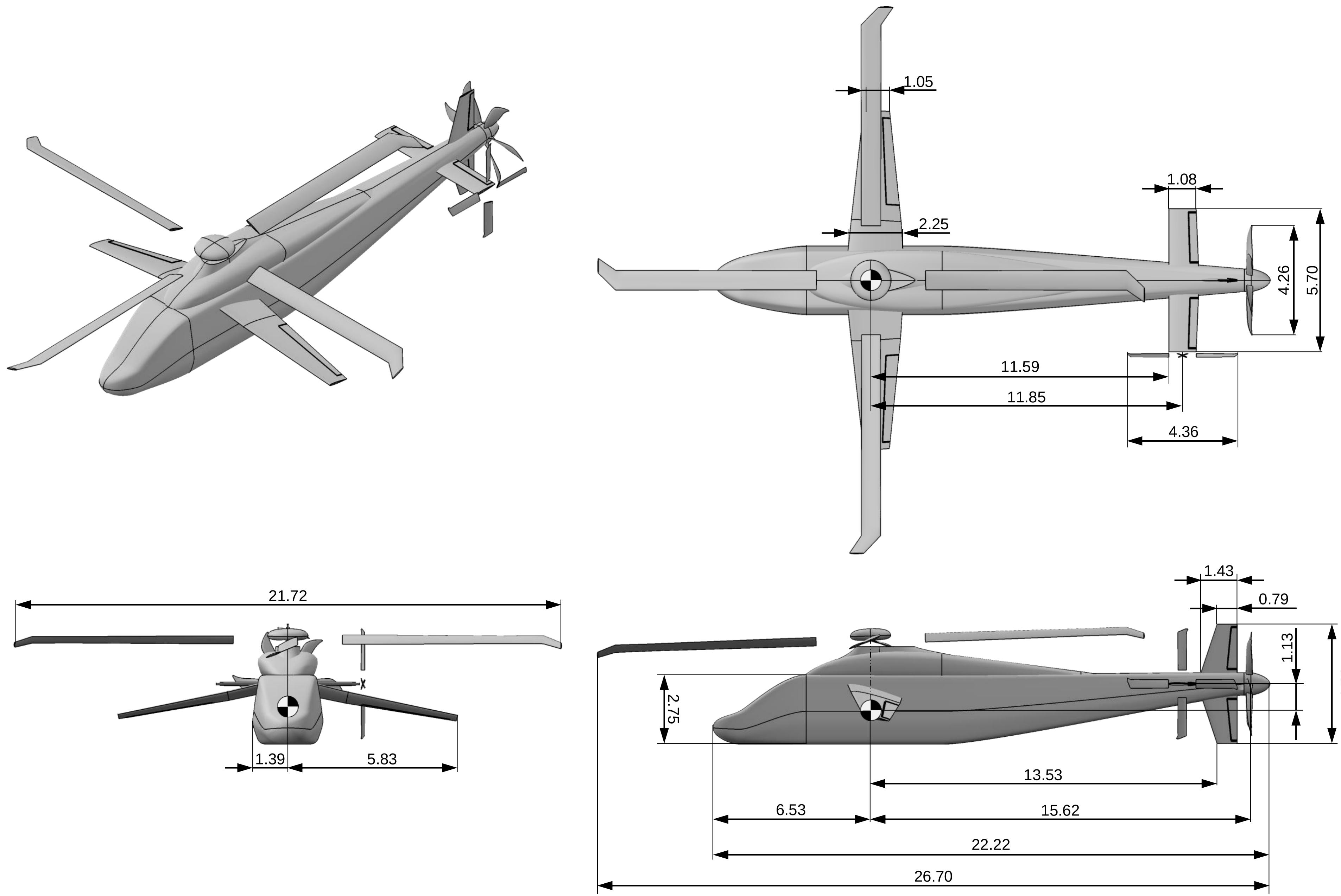

Figure 3: Four-view image of the sized high-speed rotorcraft (HSR) configuration. All length dimensions are given in meters.

2.2. Flight Mechanics Model

Rotors

The blade for the HSR main rotor is derived from the NATO-GR integrating OA231 and OA209 airfoils, previously applied on the 7AD rotor. The transition from the OA213 to the OA209 occurs from $0.75R$ to $0.92R$. Like the NATO-GR, the four-bladed main rotor features a disc loading of 463 N/m^2, a solidity σ = 0.00825, and a hover tip speed of 220.9 m/s. The blade twist is reduced from −15.25°/R to −7°/R to align with the aerodynamics of the unloaded rotor with a high advance ratio. The angle of incidence of the main rotor is 5°. Due to elevated airspeed and reduced main rotor speed, the advance ratio rises from $\mu = 0.37$ to $\mu = 0.71$. The four-bladed tail rotor features σ = 0.21, and an eight-bladed pusher propeller is modeled with σ = 0.3. The Pitt and Peters inflow model is applied for all rotors.

Body Aerodynamics

The modeling of the NATO-GR utilized the polar data from a comparable fuselage, scaled to meet the required drag area of 3.26 m^2. This scaling is based on the UH-60 configuration used in the NASA/Army UH-60A Airloads program, as outlined in [11]. The HSR's fuselage aerodynamics are modeled similarly to those of the NATO-GR. DLR's tool LIFTING-LINE [12] is used to estimate the aerodynamic coefficients of wings and stabilizers, including the control surfaces

Mass and Inertia

A realistic center of gravity and moments of inertia (MOI) are calculated by a reasonable placement of the individual components, such as wings, main rotor, engines, gearboxes, but also avionics and hydraulics during the design process. The arrangement of the component masses and computation of the center of gravity and the MOI is crucial for the flight model as they have a high impact on the system dynamics, e.g. the bandwidth.

The design mass of the configuration was determined during the mission-based sizing process in the previous work as described before. For the given payload, the basic empty mass including individual component masses were calculated through statistical methods outlined in [13]. The fuel mass was obtained as a sum of fuel consumed in the shown mission segments in Figure 1.

The center of gravity is obtained as

$$\begin{bmatrix} x \\ y \\ z \end{bmatrix}_{CG} = \frac{\sum m_i \begin{bmatrix} x & y & z \end{bmatrix}_i^T}{\sum m_i} \tag{1}$$

where m_i is the mass of the i-th component located at its coordinates x_i, y_i, and z_i. The center of gravity is also depicted in Figure 3.

Three different types of mass components are considered:

1. Point - mass components with a single point location and no geometric property for components that cannot be geometrically defined in the conceptual phase (e.g., avionics, hydraulics, drive system, gear, etc.),

2. Simple Geometric - mass components with rotational symmetric geometrical shapes and known textbook formulas for their MOI (e.g., engine as a representative cylinder or the fuel tank as rectangular prism),

3. Volumetric - mass components featuring arbitrary shapes with large volume (fuselage, wings, rotors).

The mass properties of the volumetric components are computed from each corresponding geometry. Here, the geometry is modeled in the form of point cloud by querying surface points from the geometry defined in CPACS (Common Parametric Aircraft Configuration Schema) [14] using the TiGL library [15]. The points of the corresponding component geometry are then meshed using triangular polygon elements. This type of meshing allows for better accuracy in computing the mass properties of curved surfaces (e.g., the fuselage and wings) at the cost of a higher number of elements compared to quadrilateral meshing.

Upon meshing, the component center of mass is calculated by

$$\begin{bmatrix} x \\ y \\ z \end{bmatrix}_{i} = \frac{\sum_{k=1}^{N_{elem}} A_k \begin{bmatrix} x & y & z \end{bmatrix}_k^T}{\sum_{k=1}^{N_{elem}} A_k} \tag{2}$$

Each volumetric body is considered as a thin-walled homogeneous structure with constant thickness. The component mass is distributed to each element in proportion to the element surface area A_k to the body surface area $\sum_{k=1}^{N_{\text{element}}} A_k$. For simple geometric and point components, no additional calculation for the center of mass is required, as the center of mass aligns with their geometric position.

The inertia of the HSR including all components is given as

$$I = \begin{bmatrix} I_{xx} & -I_{xy} & -I_{xz} \\ -I_{xy} & I_{yy} & -I_{yz} \\ -I_{xz} & -I_{yz} & I_{zz} \end{bmatrix} \tag{3}$$

where the diagonal terms denote the inertia terms about the x, y, and z axes with

$$
\begin{aligned}
I_{xx} &= \sum I_{xx,i} + m_i \left(\tilde{y}_i^2 + \tilde{z}_i^2\right) \\
I_{yy} &= \sum I_{yy,i} + m_i \left(\tilde{x}_i^2 + \tilde{z}_i^2\right) \\
I_{zz} &= \sum I_{zz,i} + m_i \left(\tilde{x}_i^2 + \tilde{y}_i^2\right)
\end{aligned} \tag{4}
$$

and the non-diagonal terms

$$
\begin{aligned}
I_{xy} &= \sum I_{xy,i} + m_i \, \tilde{x}_i \, \tilde{y}_i \\
I_{yz} &= \sum I_{yz,i} + m_i \, \tilde{y}_i \, \tilde{z}_i \\
I_{xz} &= \sum I_{xz,i} + m_i \, \tilde{x}_i \, \tilde{z}_i
\end{aligned} \tag{5}
$$

where $\tilde{x}_i = x_{\mathrm{CG}} - x_i$, $\tilde{y}_i = y_{\mathrm{CG}} - y_i$, and $\tilde{z}_i = z_{\mathrm{CG}} - z_i$.

In Equation (4) and (5), the first term represents the MOI of the i-th mass component about its own center of mass, while the second term is the expression resulting from the parallel axis theorem with respect to $[x\,y\,z]_{\mathrm{CG}}^T$. These equations are used in the given form for volumetric and geometric components, while for the point mass components, the MOI is obtained only from the parallel axis term of the equations above. The overall MOI of the volumetric components is calculated from its meshed elements. Here, the inertia of each meshed element is calculated on the 2D-plane and transformed into 3D-space with respect to the normal vector of the triangle element.

Based on the aforementioned methodology, the determined mass properties of the HSR are listed in Table 2. Except for the tail rotor, each component lies on the x-z plane.

Table 2: Mass properties of the HSR.

Parameter	Unit	Value
x_{CG}	m	6.5
y_{CG}	m	0.0
z_{CG}	m	2.62
I_{xx}	kg m^2	64 586
I_{yy}	kg m^2	361 235
I_{zz}	kg m^2	364 103
I_{xy}	kg m^2	−11 025
I_{yz}	kg m^2	7855
I_{xz}	kg m^2	176

Control Inputs and Trim Laws

The HSR features a total of ten control inputs:

- main rotor longitudinal cyclic δ_x,
- main rotor lateral cyclic δ_y,
- main rotor collective δ_0,
- tail rotor collective δ_p,
- pusher propeller collective δ_{thr},
- elevator on the horizontal stabilizer δ_{ele},
- rudder on the vertical stabilizer δ_{rud},
- symmetrical deflection of the flaperons δ_{flp},
- asymmetrical deflection of the flaperons for aileron operations δ_{ail},
- and a main rotor speed $\delta_{\omega_{\mathrm{MR}}}$.

Depending on airspeed, all or a subset of these controls are used. The main and tail rotors are essential for rotorcraft control from hover up to mid-speed ranges. The aerodynamic flaps are only effective at higher speeds, where the main rotor speed is reduced. The pusher can be used across the entire flight envelope.

The flight mechanical model of the sized HSR is trimmed between hover and 260 knots in level flight with a 10 knots spacing. To account for different vehicle characteristics in the flight envelope, four different trim laws are considered:

I At low airspeeds, the main rotor has maximum authority. The HSR is trimmed using the conventional helicopter controls δ_x, δ_y, δ_p, and δ_0. In forward flight, pusher propeller collective δ_{thr} is adjusted accordingly to cancel out the thrust resulting from the free-stream inflow. Therefore, δ_{thr} is larger than zero.

II From 97 knots (50 m/s) onward, the second trim law sets the resulting angle of attack α of the fuselage to zero in order to slowly off-load the main rotor through additional pusher propeller thrust using δ_{thr}.

III From 138 knots (71 m/s) onward, the ailerons (asymmetrical wing flap deflections) δ_{ail} are additionally used to off-load the main rotor around the roll axis. The aileron position is adjusted linearly from hover to 138 knots to avoid control jumps.

IV The last trim law takes effect from 196 knots (101 m/s) onward and additionally off-loads the main rotor around the pitch axis by utilizing the elevator δ_{ele} and flaps δ_{flp}.

During trim laws III and IV, the main rotor speed $\delta_{\omega_{\mathrm{MR}}}$ is reduced according to the increasing airspeed. The rudder is not required for trimming. The trim controls and important helicopter states are shown in Figure 4.

2.3. Linear Models

The HSR model is linearized within HOST at all trim points to obtain linear state-space models according to the corresponding trim law. The state-space models include 20 model states:

- 9 rigid body states (3 translational velocities, 3 rotational rates, 3 attitude angles),
- 6 main rotor flapping states (main rotor lag dynamics are omitted in the current model),
- 3 main rotor inflow states,
- 1 tail rotor inflow state,

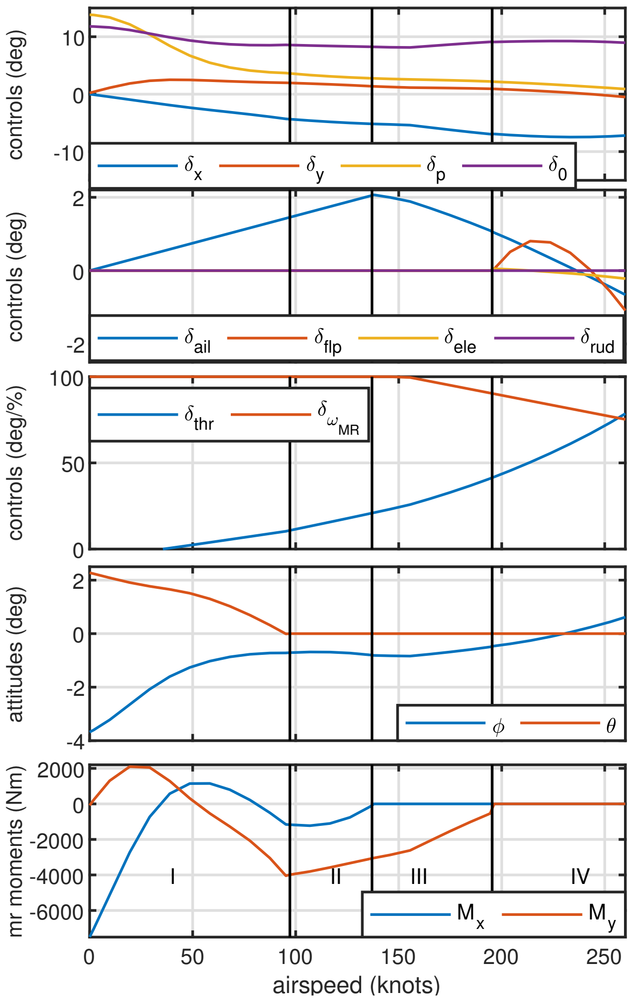

Figure 4: HSR trim values of controls, attitude angles, and main rotor moments as a function of airspeed.

- 1 pusher propeller inflow state,

and ten control inputs $\boldsymbol{\delta}$ as described at the end of Section 2.2:

$$\boldsymbol{\delta} = (\delta_x, \delta_y, \delta_p, \delta_0, \delta_{\text{thr}}, \delta_{\text{ail}}, \delta_{\text{flp}}, \delta_{\text{ele}}, \delta_{\text{rud}}, \delta_{\omega_{\text{MR}}}) \tag{6}$$

Furthermore, all linear models include the necessary outputs for flight control design and model analysis, such as angle of attack α, sideslip angle β, and the corresponding rates, as well as vertical velocity v_z, and the required aircraft power P_{required}.

Eigenvalues The eigenvalues of the linearized state-space models as a function of airspeed (blue for low speed, bright yellow for high speed) are depicted in Figure 5 and in Figure 6 as a zoomed-in view.

The progressive, collective, and reactionless main rotor flap modes vary with airspeed (and rotor speed) as expected. All rotor modes are stable across the entire flight envelope, but the rotor model currently used by the HSR lacks the coupled lead-lag motion. Furthermore, three main rotor inflow modes are visible throughout the whole airspeed envelope. The tail rotor and pusher inflow modes also vary with the airspeed and can be found at significantly higher frequencies on the real axis.

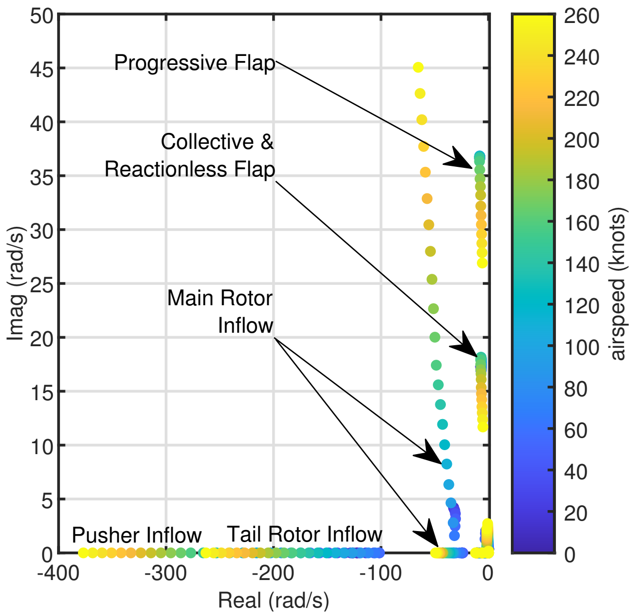

Figure 5: HSR Eigenvalues at trimmed airspeeds.

Figure 6 shows the low-frequency eigenvalues of the HSR as a function of airspeed. From hover to 110 knots, the HSR shows an unstable complex phugoid mode, and the spiral mode remains stable at these airspeeds. At higher airspeeds, the phugoid moves into the stable half-plane, while the spiral becomes unstable. Furthermore, a very low-frequency pusher mode can be found, which is strongly coupled with the spiral mode of the HSR. A coupled heave and yaw subsidence mode lies in the stable half-plane. The Dutch roll is stable but lightly damped, and its frequency increases as airspeed increases. Additionally, two fuselage-coupled regressive flap modes are located at lower frequencies denoted as pitch-flap and roll-flap. At low airspeeds, two pitch-flap eigenvalues lie on the real axis and become a complex pole pair with increasing frequency at higher speeds. The opposite behavior is observed for the roll-flap mode: For low airspeeds, the roll-flap poles are complex and move to the real axis, with frequency increasing with airspeed.

Stability and Control Derivatives The effective rigid body stability and control derivatives are shown as a function of airspeed in Figure 14 and Figure 15 at the end of the paper. The rigid body derivatives are determined from the reduced (rigid body) models by applying the singular perturbation method. This approach, as described in [16], assumes that the high-order dynamics are significantly faster than the rigid

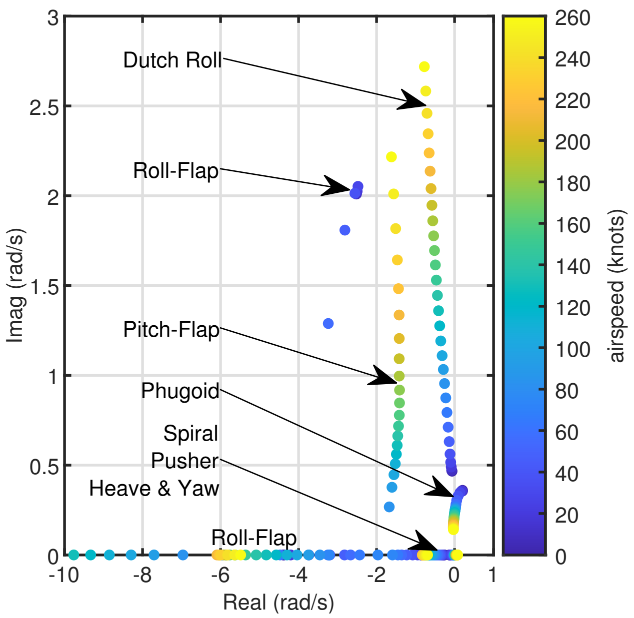

Figure 6: Eigenvalues at trimmed airspeeds (zoomed-in).

body dynamics.

The on-axis damping derivatives L_p, M_q, and N_r shown in Figure 14 rule the dynamics of the respective axes for low and medium airspeeds. While M_q and N_r increase with increasing airspeed, L_p decreases and reaches the same order of magnitude as L_q and L_r at higher speeds. As a result, the coupling effects on the roll axis increase with increasing airspeed.

The dihedral derivative L_v and the weathercock stability N_v determine lateral/directional static stability. While the positive N_v has a stabilizing effect, L_v changes its sign from negative to positive at around 160 knots and thus has a destabilizing effect. Surprisingly, the spiral mode of the HSR is already unstable from 110 knots onwards.

The on-axis roll control derivative L_{δ_y} depicted in Figure 15 decreases significantly above 160 knots, while at the same time, the coupling derivative L_{δ_x} increases. The coupling derivative from collective to roll L_{δ_0} is also very pronounced from approximately 140 knots onwards. For this reason, the main rotor control is greatly reduced at high airspeeds. Aileron effectiveness $L_{\delta_{\text{ail}}}$ increases with V_{tas}^2 and reaches a similar order of magnitude as L_{δ_y} upwards of approximately 200 knots. Furthermore, the coupling of pusher to roll $L_{\delta_{\text{thr}}}$ does not appear to be particularly large but should be taken into account to compensate for the resulting roll moment for pusher propeller inputs.

The main control derivative in pitch M_{δ_x} is significantly smaller than that in roll L_{δ_y}, which is to be expected. M_{δ_x} increases with velocity, while the coupling derivative M_{δ_y} decreases. A similar observation was also made for the winged single main rotor helicopter study in [6]. Naturally, M_{δ_0} increases strongly with velocity and is similar to M_{δ_x} from about 160 knots onwards. For higher speeds, the elevator becomes the main pitch control and reaches the same effectiveness as longitudinal cyclic δ_x at round 240 knots.

In hover, the yaw axis control derivative clearly shows a coupling from collective to yaw, but the corresponding derivative N_{δ_0} decreases at higher speeds. Both the aileron coupling derivative $N_{\delta_{\text{ail}}}$ and the rudder derivative $N_{\delta_{\text{rud}}}$ increase with V_{tas}^2. At 160 knots, tail rotor effectiveness is about three times that of rudder effectiveness.

The collective control derivative Z_{δ_0} is dominant along the vertical axis up to approximately 160 knots, after which strong couplings occur due to a larger Z_{δ_x} derivative. The control derivatives of the (symmetrical) flaps $Z_{\delta_{\text{flp}}}$ are about twice as large as $Z_{\delta_{\text{ele}}}$, but do not have the same order of magnitude as the collective. For this reason, the vertical axis is controlled indirectly via pitch control at higher airspeed, like in fixed-wing aircrafts.

Thrust via pusher $X_{\delta_{\text{thr}}}$ is clearly recognizable and increases with speed. X_{δ_x} also generates thrust, but not independently of a pitch moment. Lateral forces cannot be generated independently of the roll axis.

3. FLIGHT CONTROL ARCHITECTURE

The flight control system is developed using the linearized models of the HSR for the entire speed range up to 260 knots. An explicit model-following (EMF) control system architecture [17], with modifications for an overactuated, high-speed vehicle as described in [4], is used. The EMF flight control architecture of the HSR is shown in overview form in Figure 7 and consists of six main components: command model and command delays, feedforward, feedback, transformation to the body system, and control allocation. These components, along with actuator and sensor dynamics, as well as, time delays, are described in detail in the following sections.

3.1. Command Model and Delays

The command model generates proper reference values from pilot inputs for the feedback and feedforward controllers. Therefore, the command model is essential for setting the response behavior of the overall flight control system, as it specifies response type, bandwidth, and magnitude. The implemented command model of the HSR switches its response types automatically with airspeed or by the pilot's request, depending on the axis. All response types are shown in Table 3 as a function of airspeed.

In the longitudinal axis, a Rate Command / Attitude

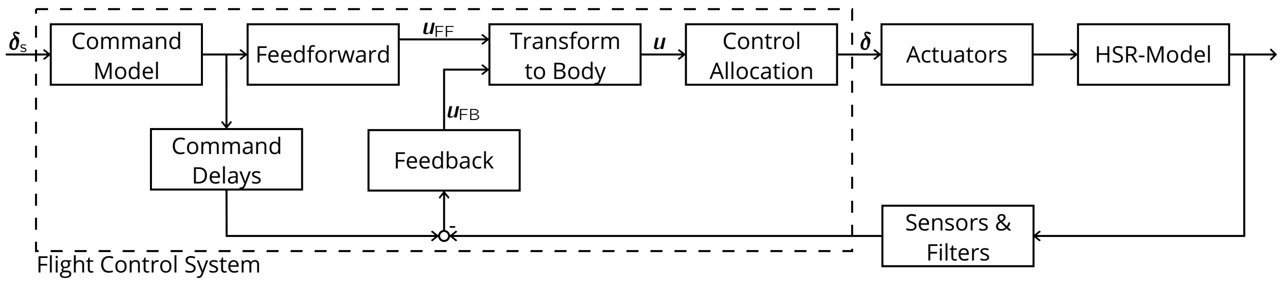

Figure 7: Overview of the EMF flight control system architecture.

Table 3: HSR command model response types with respect to airspeed.

<table>
<tr><th>Airspeed (knots)</th><th>Collective</th><th>Longitudinal Cyclic</th><th>Lateral Cyclic</th><th>Pedals</th></tr>
<tr><td>0 - 20</td><td rowspan="2">Direct Collective,
Vertical Speed Command
or
Thrust Command /
Airspeed Hold</td><td rowspan="3">Attitude Command /
Attitude Hold
(ACAH)
or
Rate Command /
Attitude Hold
(RCAH)</td><td rowspan="3">Attitude Command /
Attitude Hold
(ACAH)
or
Rate Command /
Attitude Hold
(RCAH)</td><td>Rate Command (RC)</td></tr>
<tr><td>20 - 80</td><td>Rate Command /
Turn Coordination
(RCTC)</td></tr>
<tr><td>80+</td><td>Thrust Command /
Airspeed Hold</td><td>Sideslip Command /
Turn Coordination</td></tr>
</table>

Hold (RCAH) response type with a first-order command model is implemented using

$$\frac{q_{cm}}{\delta_{x_s}} = \frac{K_{x,RC}\omega_{x,RC}}{s + \omega_{x,RC}} \tag{7}$$

The RCAH can be switched by pilot request to an Attitude Command / Attitude Hold (ACAH) response type with the underlying second-order model

$$\frac{\theta_{cm}}{\delta_{x_s}} = \frac{K_{x,AC}\omega_{x,AC}^2}{s^2 + 2\zeta_{x,AC}\omega_{x,RC}s + \omega_{x,RC}^2} \tag{8}$$

RCAH and ACAH are available throughout the full flight envelope for the longitudinal axis and also for the lateral axis with different time constants.

Pedal command types switch automatically with airspeed: Between hover and 80 knots, a first-order rate command (RC) model is implemented, as seen in Equation (7). The RC is enhanced by Turn Coordination (TC) between 20 and 80 knots. For airspeeds greater than 80 knots, Sideslip Command / Turn Coordination applies a second-order command model.

The collective stick features two different response types that are also selectable by the pilot. In addition to direct control of the main rotor collective (direct), a Vertical Speed Command & Hold and a Thrust Command / Airspeed Hold are available, both using an underlying first-order model. Above 120 knots, only the Thrust Command / Airspeed Hold mode is available and the Airspeed Hold can be activated by the pilot.

All command model parameters are fixed throughout the full flight envelope and are set to meet ADS-33E Level 1 handling qualities (Target Acquisition & Tracking) [18]. Additionally, command delays are used to delay the command model reference values before comparing them with the actual measurements, which is usually done in EMF control architectures. The command delays represent high-order effects or delays that are not modeled in the actual command model like actuators and sensors dynamics or processing delays. For the HSR, all axes share the same command delay of 96 ms.

3.2. Feedforward

The main purpose of feedforward control is to accelerate the initial response of the aircraft and thus increase the bandwidth of the flight control system. Ideally, the feedforward control generates control inputs sufficient to guide the aircraft to the reference values generated by the command model. As the control allocation already performs static decoupling, only the main axes (including the control allocation) are considered for feedforward design. Therefore, low-order single-input/single-output transfer functions at each trim point are fitted on the corresponding on-axis in a frequency range between 1 and 10 rad/s to estimate the feedforward parameters. Consequently, the feedforward parameters are airspeed scheduled.

The pitch and roll axes can be mapped sufficiently well over the entire speed range using a second-order system. The feedforward transfer function for the cyclic axes has the form

$$\frac{y}{u} = \frac{K\left(s + \frac{1}{T_z}\right)}{(s + p_1)\,(s + p_2)} \tag{9}$$

with K, p_1, and p_2 to be optimized and an additional zero with the time constant T_z = 40 ms to realize the inverse transfer function in the flight control system. The fit of the feedforward transfer function given in Equation (9) for the roll rate p/u_p in hover is shown in Figure 8. The feedforward model fit between 1 and 10 rad/s is considered as excellent.

The yaw rate feedforward is represented by a first-order system of the form

$$\frac{y}{u} = \frac{K}{s + p_1} \tag{10}$$

for which no additional zero is required to realize the inverse. For high airspeeds, the feedforward control is generated by the sideslip angle β featured by a second-order system.

The vertical axis is represented by a first-order system like in Equation (10). No feedforward is provided for pusher thrust. Hence, the feedforward controls are denoted as

$$\boldsymbol{u}_{\mathrm{FF}} = \begin{pmatrix} u_{\mathrm{FF},w} & u_{\mathrm{FF},p} & u_{\mathrm{FF},q} & u_{\mathrm{FF},r} \end{pmatrix}^T . \tag{11}$$

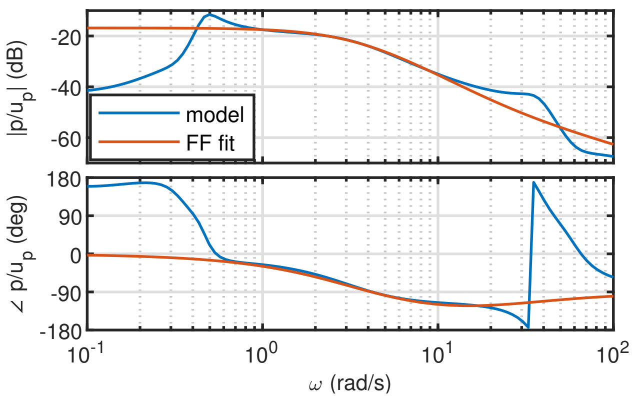

Figure 8: Roll axis p/u_p feedforward model fit in hover.

3.3. Feedback

The feedback controller compensates the errors caused by a non-precise feedforward, unconsidered couplings, higher-order model components, and disturbances, in order to keep the measurements as close as possible to the commanded values. The gains used for each controller axis are described below.

- Longitudinal and lateral cyclic feedback uses rate error ($e_{\dot\phi}$ and $e_{\dot\theta}$ respectively), attitude error (e_ϕ and e_θ), and attitude error integral feedback gains.
- Yaw rate feedback at hover and low speeds is realized by yaw rate error e_r, and rate error integral feedback. At higher airspeeds, sideslip control is activated, which uses the error of angle β, and the corresponding integral feedback gains.
- The vertical axis is stabilized using error of the vertical velocity v_z, and its integral feedback.
- Thrust command is realized by direct control of the pusher collective using the (filtered) collective stick around the pusher trim. The airspeed hold mode uses the error of airspeed V_{tas}, and the corresponding integral feedback gains.

Additionally, each controller output features a lead compensator to increase phase margin and a dedicated roll-off filter. Overall, 20 controller gains and time constants determine the feedback component. The feedback controls are denoted as

$$\boldsymbol{u}_{\mathrm{FB}} = \begin{pmatrix} u_{\mathrm{FB},V_{\mathrm{tas}}} & u_{\mathrm{FB},v_z} & u_{\mathrm{FB},\dot\phi} & u_{\mathrm{FB},\dot\theta} & u_{\mathrm{FB},r} \end{pmatrix}^T \tag{12}$$

Feedback tuning specifications, details of the optimization used, and the tuning results can be found in Section 4.

3.4. Transformation to the Body System

The designed feedforward control is based on the linear models in the body-fixed coordinate system using the rotational rates p and q and their derivatives, since the main rotor and the control surfaces of the HSR generate moments in the body-fixed frame. The longitudinal and lateral feedback control, on the other hand, are designed using the earth-fixed Euler angles ϕ and θ to realize an appropriate attitude hold. A simple sum of the feedback and feedforward outputs leads to undesirable coupling between pitch, roll, and yaw, especially during pitch or yaw maneuvers at large bank angles. This is avoided by transforming the longitudinal and lateral feedback controls into the body-fixed coordinate system. To do this, the feedback and feedforward controls are transformed to generate the control allocation inputs $\boldsymbol{u}$

$$\begin{pmatrix} u_u \\ u_w \\ u_p \\ u_q \\ u_r \end{pmatrix} = \begin{pmatrix} 1 & 0 & 0 & 0 & 0 \\ 0 & 1 & 0 & 0 & 0 \\ 0 & 0 & 1 & -\tan_\phi \tan_\theta & \tan_\theta / \cos_\theta \\ 0 & 0 & 0 & 1/\cos_\phi & \tan_\phi \\ 0 & 0 & 0 & 0 & 1 \end{pmatrix} \cdot \begin{pmatrix} u_{\mathrm{FB},V_{\mathrm{tas}}} \\ u_{\mathrm{FB},v_z} \\ u_{\mathrm{FB},\dot\phi} \\ u_{\mathrm{FB},\dot\theta} \\ u_{\mathrm{FB},r} \end{pmatrix} + \begin{pmatrix} 0 \\ u_{\mathrm{FF},w} \\ u_{\mathrm{FF},p} \\ u_{\mathrm{FF},q} \\ u_{\mathrm{FF},r} \end{pmatrix} = \boldsymbol{u} \tag{13}$$

3.5. Control Allocation

A control allocation is required for the HSR in order to distribute the demanded forces and moments

$\boldsymbol{u} = (u_u, u_w, u_p, u_q, u_r)^T$ to the various actuators $\boldsymbol{\delta}$. In this paper, a weighted pseudo-inverse method, as described in [19], is applied to calculate the control allocation matrix depending on the airspeed

$$\boldsymbol{\delta} = \boldsymbol{W}^{-1}\hat{\boldsymbol{B}}_{\text{rb}}^{T}\left(\hat{\boldsymbol{B}}_{\text{rb}}\boldsymbol{W}^{-1}\hat{\boldsymbol{B}}_{\text{rb}}^{T}\right)\boldsymbol{u} \tag{14}$$

The input matrix $\hat{\boldsymbol{B}}_{\text{rb}}$ used to calculate the control allocation is composed of the rows (u, w, p, q, r) of the rigid body control derivative matrix $\boldsymbol{B}_{\text{rb}}$ calculated in Section 2.3. Each column is normalized by the reference control derivatives $\left(X_{\delta_{\text{thr}}}, Z_{\delta_0}, L_{\delta_y}, M_{\delta_x}, N_{\delta_p}\right)$ from the 90 knots-model in order to keep the gains of the control allocation matrix interpretable accordingly. A sideward force is not accounted for in the control allocation as it cannot be generated independently of the roll moment. All actuator signals, except the main rotor speed, are used in the control allocation.

The diagonal weighting matrix $\boldsymbol{W}$ is used to reduce the couplings caused by the loaded main rotor at high speeds, as described in Section 2.3. Therefore, the corresponding main rotor and tail rotor weighting coefficients in $\boldsymbol{W}$ are exponentially reduced between 120 knots and 235 knots. The main rotor weight and selected coefficients of the control allocation matrix for the roll axis are shown in Figure 9.

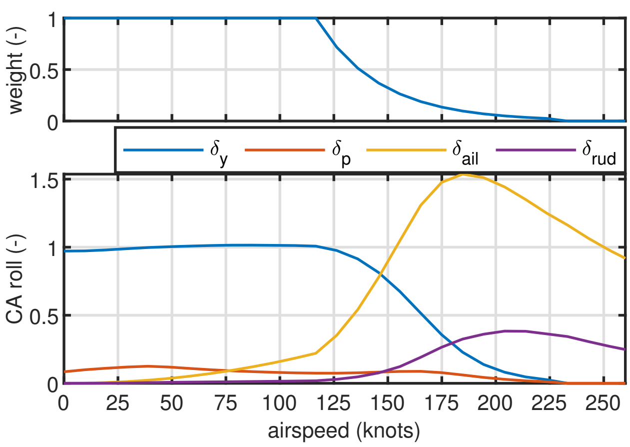

Figure 9: Main rotor weight and roll CA coefficients.

As can be clearly seen in the lower graph of Figure 9, δ_y is around 1 for low airspeeds. The control allocation for δ_y has a gain of 1 and it is therefore the main lateral control, since all others control coefficients are small. The aileron and rudder gains δ_{ail} and δ_{rud} are low until 120 knots as the flap efficiency is very low due to low dynamic pressure. After 120 knots, the aileron and rudder gains increase significantly while the lateral cyclic δ_y and tail rotor δ_p gains decrease. The main rotor weight is reduced as shown in the upper graph. At around 180 knots, the aileron needs to be amplified by a factor of 1.5 in order to generate the same rolling moment as lateral cyclic does at low airspeeds.

3.6. Actuators, Sensors, and Filters

For a realistic design of a flight control system, all time delays of the closed-loop system must be taken into account during the flight control design and later in the simulation. Since the nonlinear and linear models solely include the flight mechanics of the bare airframe, additional actuator dynamics, sensor and filter dynamics, as well as transmission time delays, are required for a proper estimation of the overall time delay. To ensure comparability with the analyzed high-speed configuration from [4], the time constants are based on this publication with minor modifications.

As a result, the actuator model is designed as a second-order model with position and rate limits, and a time constant ω_{act} = 50 rad/s, a damping ratio ζ_{act} = 0.7, and a time delay τ_{act} = 8 ms, which corresponds to the sampling time used in the HSR simulation. The pusher propeller collective actuator has a lower time constant of ω_{thr} = 25 rad/s. The sensor modeling follows Ref. [4] to account for sensor dynamics, and possible notch, anti-aliasing and structural filters. They are modeled as second-order systems with a time constant ω_{sensor} = 30 rad/s and a time delay τ_{sensor} = 16 ms.

4. TUNING RESULTS AND ASSESSMENT

The feedback gains and the time constants of the lead compensators and roll-off filters are optimized using the multi-model and multi-objective functionality of the fixed-structure, non-smooth $\mathcal{H}_\infty$ tuning algorithms [20], provided by MATLAB *systune* [21]. Since the applied optimization objectives (referred to as "goals") differ from the well-known CONDUIT [17], which directly incorporates ADS-33E criteria [18], these goals are described in detail to show their relevance.

4.1. Tuning Goals

MATLAB *systune* distinguishes between hard and soft tuning goals. The hard goals are prioritized and minimized until they are fulfilled. The soft goals are minimized afterwards, with the aim of ensuring that the hard goals continue to be met. The stability margin, sensitivity, gain, and minimum loop gain goals are defined as hard goals for the optimization of HSR controllers. Only step tracking is defined as a soft goal to minimize the deviation between the command model references and the actual measurements.

Stability Margin The tuning goal *margins* specify minimum stability disk-based margins [22]. As disk-based margins consider simultaneous gain and phase variations, they are more conservative than classi-

Table 4: Selected tuning goals for HSR flight control optimization.

Tuning Goal	Description	Axis
	Hard Goals	
Margins	gain and phase (disk) stability margins	all
Sensitivity	sensitivity shape for	all
	- disturbance rejection bandwidth and peak	
	- steady state error	
MinLoopGain	minimum crossover frequency for robustness	all
(Maximum) Gain	thrust-roll coupling	roll
	Soft Goals	
StepTracking	command model following costs	all

cal gain and phase margins as supported in CONDUIT. Nonetheless, the standard stability margin values (6 dB, 45 deg) are enforced in this paper for all axes with the feedback broken at the control allocation $\boldsymbol{u} = (u_u, u_w, u_p, u_q, u_r)^T$.

Sensitivity The disturbance rejection bandwidth (DRB) and disturbance rejection peak (DRP) criteria as proposed in [23] can be directly defined by specifying the *sensitivity* goal. This way, the free parameters are tuned to limit the sensitivity at a broken loop insertion point (here: the angle or velocity disturbances) below a specified weighting function. The maximum roll-axis sensitivity function including the sensitivity of all airspeeds are shown in Figure 10. The used weighting function has a maximum of 5 dB gain for mid to high frequency to fulfill the DRP criterion, and passes −3 dB at ω_{DRB} to meet the DRB criterion. In addition, the deviation from the steady-state response is limited by the drop-in sensitivity in the low-frequency range. As the *sensitivity* goal is specified as hard goal, the sensitivity of all models are below the maximum sensitivity function. For each axis, a dedicated sensitivity goal is applied.

Gain The designed control allocation already significantly reduces the coupling of pusher thrust to the roll axis, but undesirable roll moments can still be observed with strong changes in thrust, which should be further reduced by the (maximum) *gain* goal. The *gain* constraint is used to tune the free parameters so that the gain from the chosen input to the output is less than or equal to a specified transfer function $W(s)$. To reduce the coupling of pusher thrust to rolling moment, the following transfer function from the thrust input to the measured roll angle below 0.05 rad/s is used for this purpose

$$W_{\mathrm{thr},\phi}(s) = -65\,\mathrm{dB}\,\frac{\frac{1}{0.05}s}{\frac{1}{0.05}s + 1} \tag{15}$$

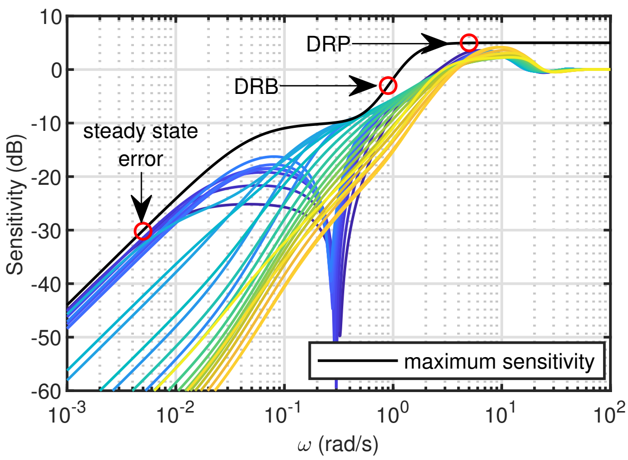

Figure 10: Maximum sensitivity tuning goal and sensitivity of all models (colors indicate airspeed).

Minimum Loop Gain The minimum crossover frequency specification to ensure robustness against model variants cannot be directly mapped into the *MinLoopGain* goal in *systune*, as MATLAB does not limit the open-loop frequency response $\boldsymbol{L}$, but the inverse of its sensitivity function $\boldsymbol{S}^{-1} = (\boldsymbol{I} + \boldsymbol{L})$. This simplification is not valid for $\boldsymbol{L} \approx 0$, but it is found to be a low threshold solution to shift the minimum crossover frequency to higher frequencies.

Step Tracking The *Step Tracking* goal seeks to minimize the error between the command model reference and the sensor measurements. Here, a separate goal is defined for each axis. In this paper, the *step tracking* goals are used as soft goals, meaning that they are minimized until a maximum number of iterations or a relative tolerance is reached.

Table 4 summarizes the selected hard and soft tuning goals and the axes to which they are applied. Further goals are "checked only" after the optimization, but are not included in the optimization as goals. These include the position of the eigenvalues according to the ADS-33E criterion on pitch (roll) oscillations and the maximum crossover frequency for evaluating the actuator activity.

In addition, a large number of ADS-33E [18], its proposed revision [23], MIL-STD-1797B, and further updated criteria for evaluating controller and handling qualities have been implemented. These criteria cannot be optimized directly with MATLAB *systune*, but are checked after optimization. A selection is presented in the following section.

4.2. Optimization and Results

As described in Section 3.3, a total of 20 controller parameters are optimized. The controller parameters are gain-scheduled for each trimmed airspeed from hover to 260 knots with 10 knots increments, for a total of 28 design models. In the first run, each airspeed is optimized individually. The resulting controller parameters are then interpolated by a polynomial with an appropriate degree. For the second optimization run, the feedback parameters are defined as polynomial surfaces w.r.t. airspeed using an estimated degree and the initial value from the first run. Hence, a smooth variation of the controller parameters with airspeed is achieved. The optimized feedback gains of the pitch axis are depicted as a function of airspeed in Figure 11.

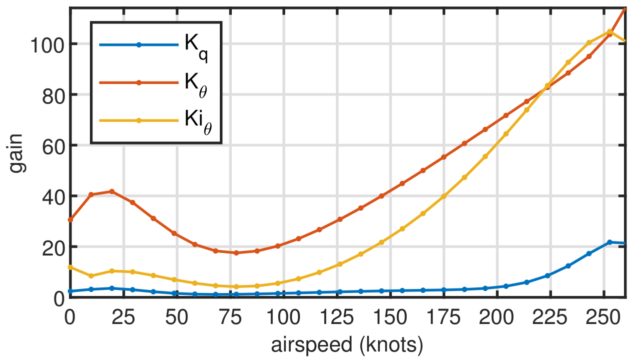

Figure 11: Pitch feedback gains as a function of airspeed.

The assessment results of the tuned flight control system of the HSR are shown in Figure 12 and Figure 13 for selected specifications. Each row of Figure 12 shows one main control axis of the HSR, i.e., roll, pitch, yaw, heave, and the thrust axis. The optimized stability margins and disturbance rejection criteria (first two columns) are met for all axes as specified. It is noticeable that the defined disturbance rejection bandwidth is clearly over-fulfilled and is not on the targeted DRB value as, for example, given in [4]. On the other hand, the targeted minimum crossover frequency cannot be successfully achieved by *systune* for all speeds. Nonetheless, it is larger than 2.5 rad/s which is the nominal guideline for conventional helicopters for the pitch and roll axis [17]. As described above, this is due to the approximation of the minimum loop gain goal used. Roll, pitch, and yaw bandwidth (4th column) are situated well within Level 1 limits (Target Acquisition & Tracking) based on ADS-33E [18] and the proposed updates [24] and [25]. The height response criterion is also predicted as Level 1. The command model bandwidth and phase delay is shown as + in the corresponding plot.

The achieved specifications shown in Figure 13 focus on pitch-axis and flight path specifications from MIL-STD-1797B and the proposed update from [24]. These criteria are evaluated using the RCAH instead of ACAH as used in Figure 12, since the estimated low-order transfer function to calculate the control anticipation parameter (CAP) assumes a rate command. The flight path versus pitch attitude bandwidth criterion is predicted Level 1 up to 160 knots, then the flight path bandwidth falls within Level 2 limits. As stated in [24], the first-order pitch rate command model results in zero dropback using the MIL-STD-1797B definition, which can be seen in the pitch attitude dropback plot. CAP predicts Level 1 to Level 2 ratings supporting the limits of flight path bandwidth criterion. Since the designed RCAH and ACAH command types are not specifically designed for flight path control. The last criteria shown here is pitch due to roll and roll due to pitch coupling, which is situated between Level 1 and 2. Especially roll due to pitch is predicted as Level 2 for low and medium airspeeds.

The requirements for large-amplitude attitude changes are predicted as Level 1 for RCAH and ACAH (Aggressive Agility). The requirements for moderate-amplitude attitude changes are also predicted as Level 1. Furthermore, yaw-collective coupling (hover and low speeds) and pitch-heave coupling in forward flight are evaluated and show Level 1 ratings. The roll performance specification and roll-sideslip coupling are also predicted as Level 1.

4.3. Preliminary Simulator Tests

HOST with the nonlinear flight mechanics model of the HSR has been implemented in the Air VEhicle Simulator (AVES) at DLR in the ACT/FHS research helicopter cockpit replica [26]. Consequently, preliminary simulator tests for the HSR have been conducted using conventional helicopter controls. Initial tests flown by test pilot indicated excellent handling qualities. Classic Mission Task Elements (MTEs), like slalom and pirouette, were executed flawlessly with minimal training However, a comprehensive quantitative and subjective evaluation involving multiple pilots performing MTEs, including newly developed tasks tailored to assess advanced configurations across the entire flight envelope, as described in [27], remains pending and will be the focus of future studies.

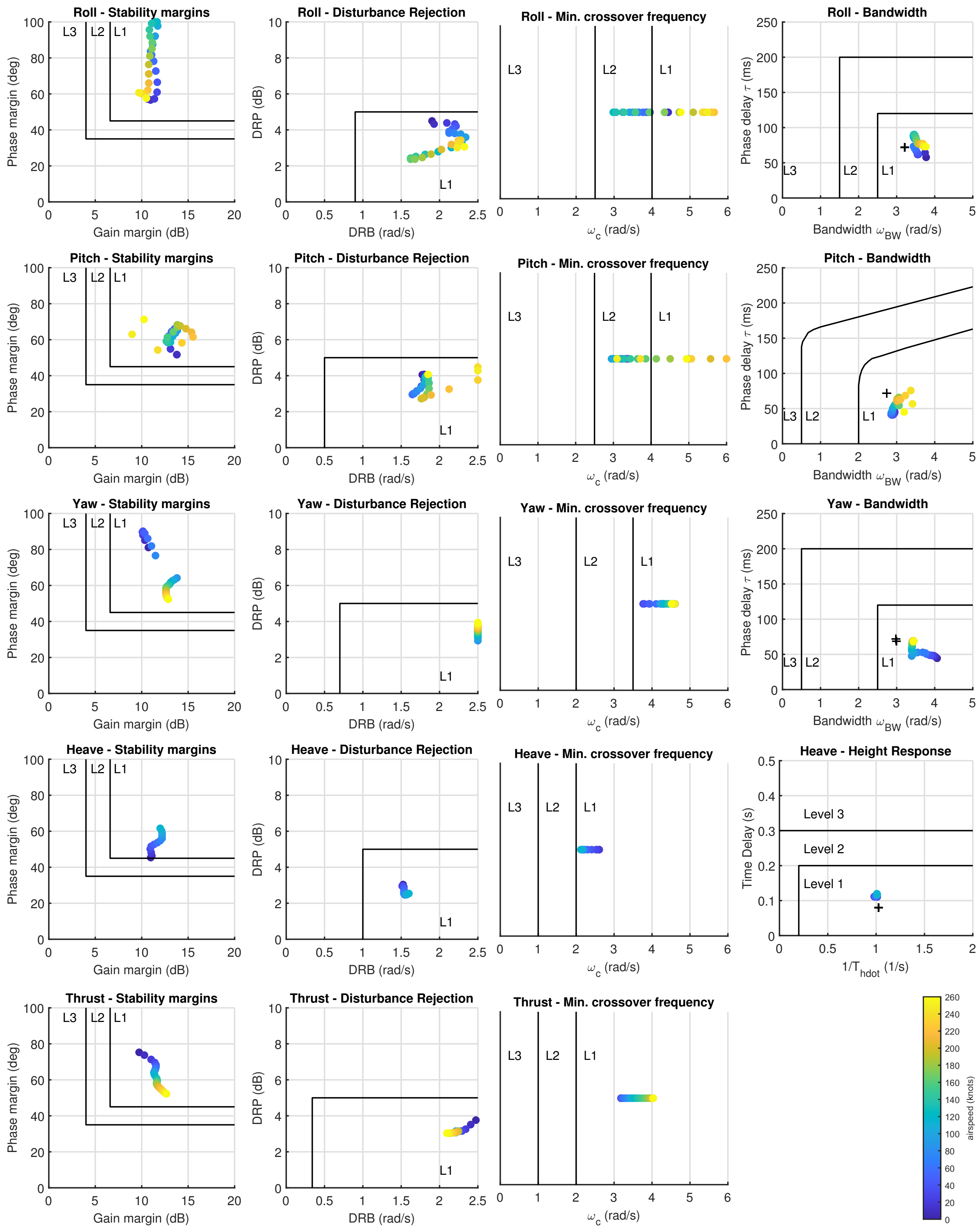

Figure 12: Achieved optimization results with respect to design specifications as a function of airspeed (ACAH).

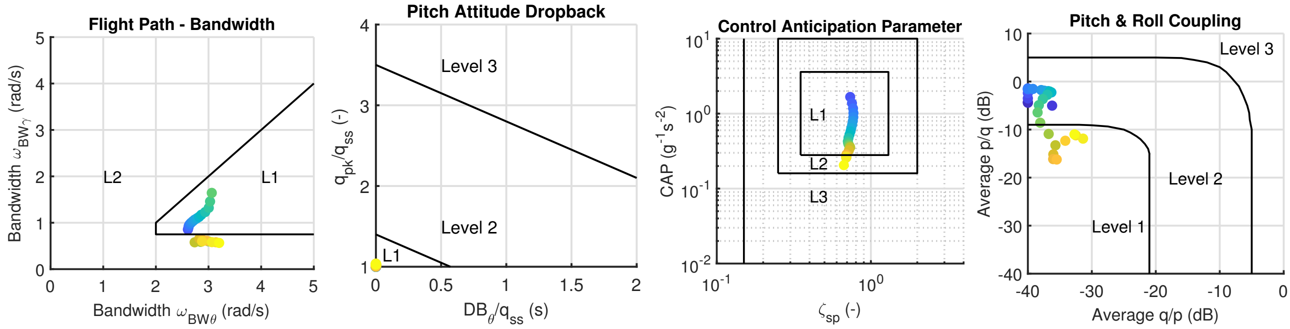

Figure 13: Achieved optimization results with respect to design specifications as a function of airspeed (RCAH).

5. CONCLUSIONS

The high-speed rotorcraft, sized and designed on the basis of a dedicated military use case, enables flight speeds above 240 knots and thus closes a capability gap of conventional helicopters. In this paper, an explicit model-following control system was designed for this high-speed compound helicopter, and controller parameters were optimized using MATLAB *systune*. This paper supports the following conclusions:

1. An iteration of the designed HSR model with regard to the actual flight mechanics is essential for the controller design and simulation. The individual components must be well-tuned to avoid any negative flight characteristics. In particular, realistic moments of inertia determines the achievable bandwidths of the flight control system.

2. In fast forward flight, the current HSR iteration shows extensive coupling between the main rotor controls, especially on the roll axis. Maneuverability can be ensured by additional aerodynamic control surfaces, but the control inputs to the main rotor must be greatly reduced at high airspeeds.

3. The selected EMF controller architecture allows for the use of different command types with otherwise identical feedforward and feedback controllers. The flight control system can be reliably designed for the entire range of flight speeds under consideration, ranging from hover to 260 knots.

4. The transfer of well-known CONDUIT specifications into MATLAB *systune* goals is partially challenging. In particular, the minimum crossover frequency cannot be satisfactorily optimized for all design points. For the most part, however, the controller assessment shows predictions within Level 1 limits.

In future work, the model of the HSR will be further refined and optimized. Wing parameters, such as the dihedral angle, and their relation to the stability of the spiral mode will be investigated. In the course of these activities, new controllers will also be designed. The flexible EMF controller architecture and optimization setup enables rapid updates. For the future piloted investigations in the AVES simulator, further adapted command model types for high-speed flight will be developed and assessed.

Author contact:
Johannes Wartmann: johannes.wartmann@dlr.de
Peter Weiand: peter.weiand@dlr.de
Kagan Atci: kagan.atci@dlr.de

References

[1] Peter Weiand, Kagan Atci, and Dominik Schwinn. High-Speed Compound Rotorcraft Performance and Design. In *Vertical Flight Society's 80th Annual Forum & Technology Display*, Montréal, Canada, May 2024.

[2] Peter Weiand, Kagan Atci, O. Schneider, S. de Graaf, L. Herzig, S. Cornelje, Dominik Schwinn, H. Inac, F. Reimer, M. Lindlar, Hennig Mainz, C. Dias Fernandes, and Richard-Gregor Becker. Development of a New Fleet Concept for HEMS Operations. In *Vertical Flight Society's 81st Annual Forum & Technology Display*, Virginia Beach, VA, USA, May 2025.

[3] Tom Berger, Ondrej Juhasz, Mark J. S. Lopez, Mark B. Tischler, and Joseph F. Horn. Modeling and control of lift offset coaxial and tiltrotor rotorcraft. *CEAS Aeronautical Journal*, 11(1):191–215, January 2020.

[4] Tom Berger, Chris L. Blanken, Jeff A. Lusardi, Mark B. Tischler, and Joseph F. Horn. Coaxial-Compound Helicopter Flight Control Design and High-Speed Handling Qualities Assessment. *Journal of the American Helicopter Society*, 67(3):98–113, July 2022.

[5] Tom Berger, Chris L. Blanken, Jeff A. Lusardi, Mark B. Tischler, and Joseph F. Horn. Tiltrotor

Flight Control Design and High-Speed Handling Qualities Assessment. *Journal of the American Helicopter Society*, 67(3):114–128, July 2022.

[6] Mark Lopez, Tom Berger, Eric Tobias, Emily Glover, and Ashwani Padthe. Seeking Lift Share: Design Tradeoffs for a Winged Single Main Rotor Helicopter. In *Vertical Flight Society's 78th Annual Forum & Technology Display*, pages 1–24, Fort Worth, Texas, May 2022. The Vertical Flight Society.

[7] Bernard Benoit, André-Michel Dequin, Konstantin Kampa, Wolfgang von Grünhagen, Pierre-Marie Basset, and Bernard Gimonet. HOST, a General Helicopter Simulation Tool for Germany and France. In *American Helicopter Society 56th Annual Forum*, Virginia Beach, Virginia, USA, 2000.

[8] Kathryn B. Hilbert. A Mathematical Model of the UH-60 Helicopter. Technical Report NASA TM 85890 and USAAVSCOM TM-84-A-2, Ames Research Center, Moffett Field, CA, USA, 1984.

[9] Axel Fink, Martin Blacha, Richard Miles, and Juan M. Jimenez García. The RACER: Manufacturing and Testing. In *47th European Rotorcraft Forum*, Virtual, United Kingdom, September 2021.

[10] Peter Weiand, Kagan Atci, and Dominik Schwinn. Analysis of High Flight Speeds on Compound Rotorcraft Design. In *51st European Rotorcraft Forum*, Venice, Italy, September 2025.

[11] Hyeonsoo Yeo, William G. Bousman, and Wayne Johnson. Performance Analysis of a Utility Helicopter with Standard and Advanced Rotors. *Journal of the American Helicopter Society*, 49(3):250–270, July 2004.

[12] Carsten M. Liersch and Tobias Wunderlich. A Fast Aerodynamic Tool for Preliminary Aircraft Design. In *12th AIAA / ISSMO Multidisciplinary Analysis and Optimization Conference*, Victoria, Canada, September 2008. Number: AIAA 2008-5901.

[13] Wayne Johnson. NDARC - NASA Design and Analysis of Rotorcraft. NASA TP 20220000355/Vol 1, Ames Research Center, Moffett Field, CA, USA, March 2022.

[14] Marko Alder, Erwin Moerland, Jonas Jepsen, and Bjorn Nagel. Recent Advances in Establishing a Common Language for Aircraft Design with CPACS. In *Aerospace Europe Conference*, Bordeaux, France, February 2020.

[15] Martin Siggel, Jan Kleinert, Tobias Stollenwerk, and Reinhold Maierl. TiGL: An Open Source Computational Geometry Library for Parametric Aircraft Design. *Mathematics in Computer Science*, 13(3):367–389, September 2019.

[16] P.V. Kokotović, R.E. O'Mallay, and P. Sannuti. Singular Perturbations and Order Reduction in Control Theory - An Overview. *IFAC Proceedings Volumes*, 8(1):512–522, August 1975.

[17] Mark B. Tischler, Tom Berger, Christina M. Ivler, Mohammadreza H. Mansur, Kenny K. Cheung, and Jonathan Soong. *Practical Methods for Aircraft and Rotorcraft Flight Control Design: An Optimization-Based Approach*. American Institute of Aeronautics and Astronautics, Inc., Reston, Virginia, USA, 2017.

[18] B. J. Baskett. *ADS-33E-PRF, Aeronautical Design Standard, Performance Specification, Handling Qualities Requirements for Military Rotorcraft*. United States Army Aviation and Missile Command, Aviation Engineering Directorate, Redstone Arsenal, Alabama, 2000.

[19] Dale Enns. Control allocation approaches. In *Guidance, Navigation, and Control Conference and Exhibit*, Boston,MA,U.S.A., August 1998. American Institute of Aeronautics and Astronautics.

[20] Pierre Apkarian, Pascal Gahinet, and Craig Buhr. Multi-model, multi-objective tuning of fixed-structure controllers. In *2014 European Control Conference (ECC)*, pages 856–861, Strasbourg, France, June 2014. IEEE.

[21] MATLAB version R2024b. The MathWorks Inc., 2024.

[22] Peter Seiler, Andrew Packard, and Pascal Gahinet. An Introduction to Disk Margins [Lecture Notes]. *IEEE Control Systems*, 40(5):78–95, October 2020.

[23] Chris L. Blanken, Mark B. Tischler, Jeff A. Lusardi, Christina M. Ivler, and Rhys Lehmann. *Proposed Revisions to Aeronautical Design Standard – 33E (ADS-33E-PRF) Toward ADS-33F-PRF*. U.S. Army CCDC AvMC, September 2019.

[24] Tom Berger, Mark B. Tischler, and Joseph F. Horn. High-Speed Rotorcraft Pitch Axis Response Type Investigation. *Journal of the American Helicopter Society*, 68(3), July 2023.

[25] Tom Berger, Anthony Gong, Jeffery A Lusardi, M Hossein Mansur, and Ryan P Boehringer. Proposed Yaw-Axis Target Acquisition and Tracking Handling Qualities Requirement Updates. In *Vertical Flight Society's 80th Annual Forum & Technology Display*, Montréal, Canada, May 2024.

[26] Holger Duda, Torsten Gerlach, Sunjoo K. Advani, and Mario Potter. Design of the DLR AVES Research Flight Simulator. In *AIAA Modeling and Simulation Technologies (MST) Conference*, Boston, Massachusetts, USA, August 2013.

[27] Tim Jusko and Tom Berger. Piloted Simulation Evaluation of MTEs for the Assessment of Low-Level Handling Qualities. In *Vertical Flight Society's 80th Annual Forum & Technology Display*, Montreal, Canada, May 2024.

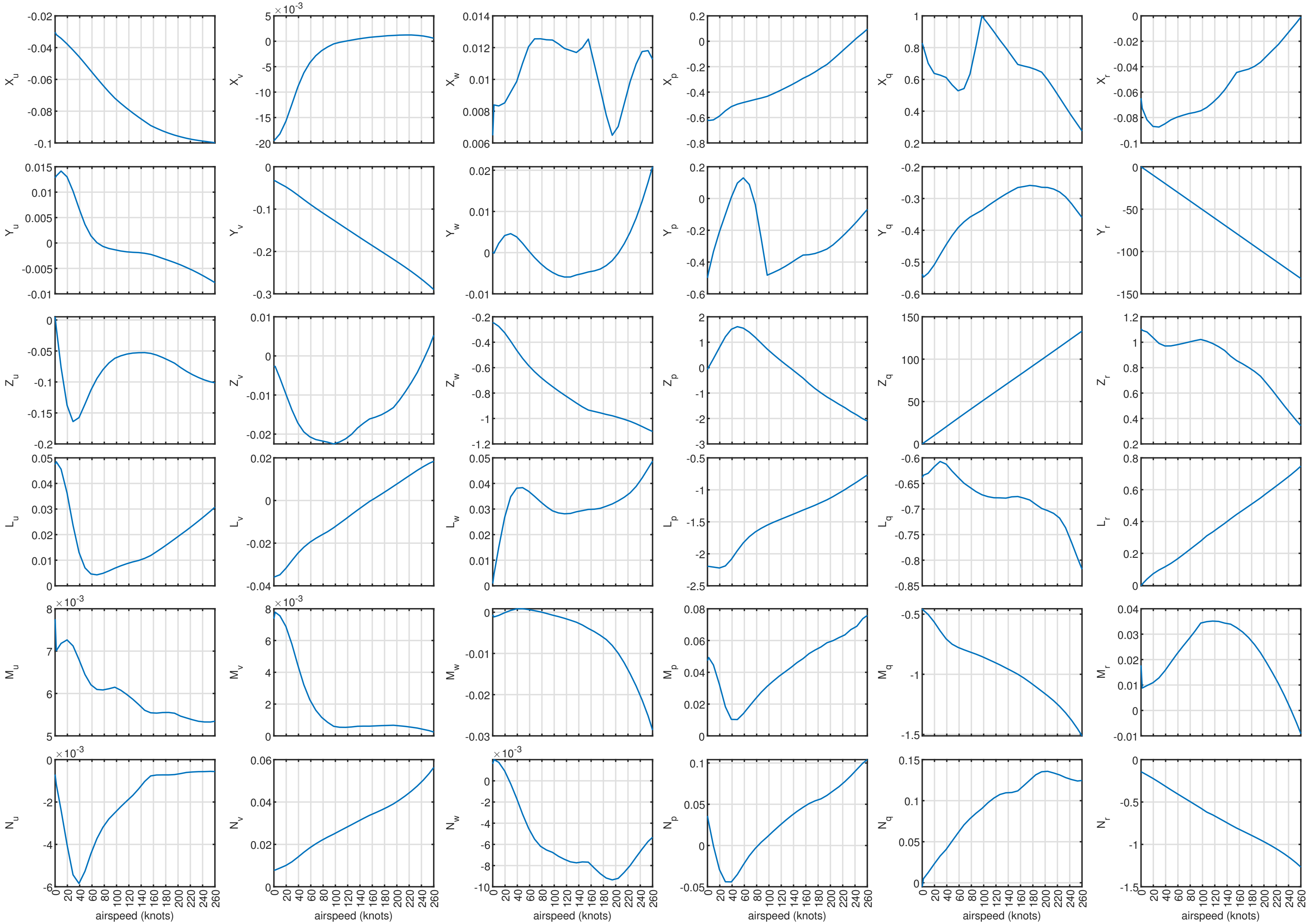

Figure 14: Effective rigid body stability derivatives as a function of airspeed of the linear HSR models.

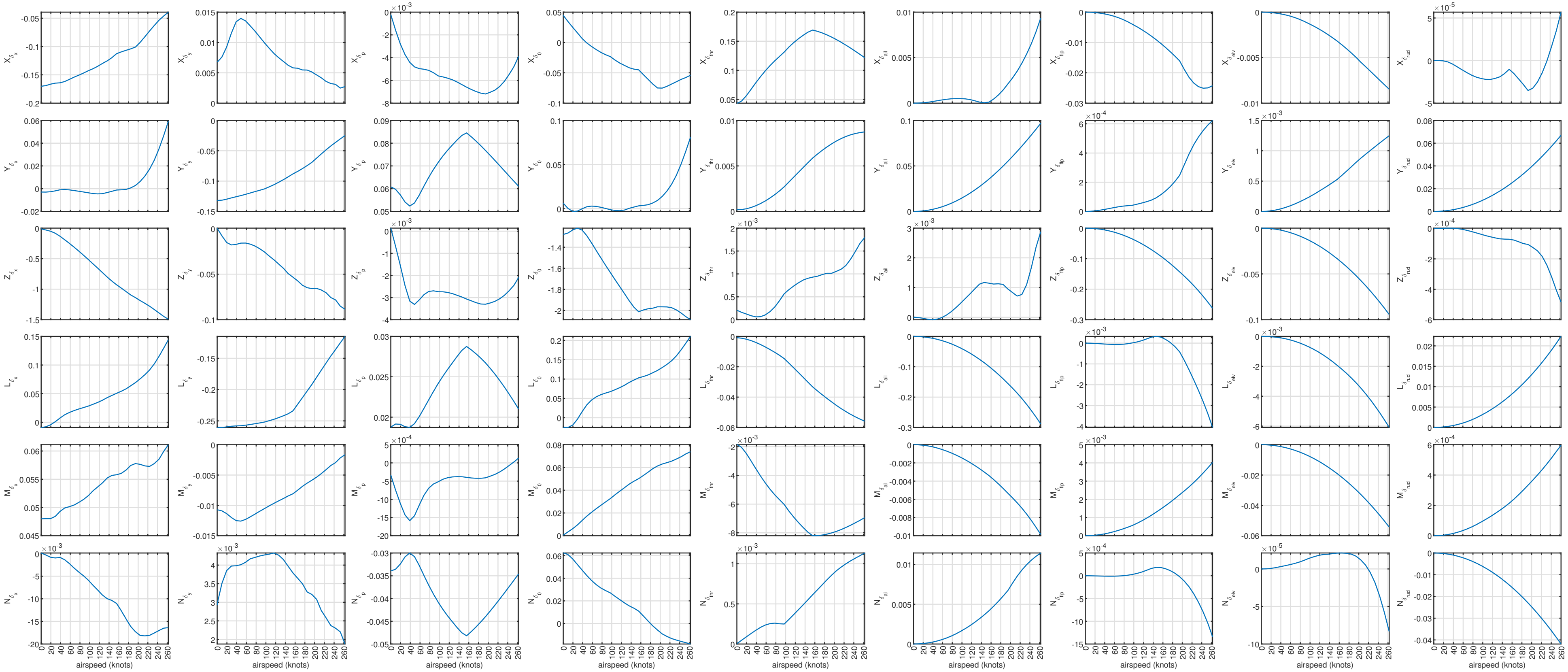

Figure 15: Effective rigid body control derivatives as a function of airspeed of the linear HSR models.